Journal of Sound and Vibration (1997) **206**(4), 541–565

A COMPARISON OF MODELS FOR THE WAVENUMBER–FREQUENCY SPECTRUM OF TURBULENT BOUNDARY LAYER PRESSURES*

W. R. GRAHAM

Department of Engineering, University of Cambridge, Trumpington Street, Cambridge, CB2 1PZ, England

(*Received* 21 *October* 1996, *and in final form* 15 *May* 1997)

Aircraft cabin noise due to the fuselage boundary layer is determined by, among other factors, the wavenumber–frequency spectrum of the fluctuating boundary layer pressures, a quantity for which a number of models have been proposed. In this work predictions for the sound radiated by a boundary layer driven plate are investigated, with a view to determining which model is most appropriate to the cabin noise problem. It is found that, for the structural and boundary layer parameters typical of transport aircraft, the contributions of resonant, acoustically inefficient plate modes dominate the radiated power. When these modes are strongly driven by the boundary layer, their excitation levels are determined by the "convective peak" of the wavenumber–frequency spectrum (where most of the fluctuation energy lies), and the radiated sound is found to be sensitive to details of the shape and location of the peak, giving differing results for models normally thought to agree at this point. Otherwise, it is the sub-convective region of the wavenumber–frequency spectrum that is important, and differences between models here lead to corresponding discrepancies in radiated sound predictions. Since the first case is generally more problematic, one can conclude that a suitable model must above all describe the convective peak accurately; however, the extent to which existing alternatives do so remains unclear.

1. INTRODUCTION

Boundary layer induced noise is already a significant contributor to cabin sound levels in the current generation of passenger aircraft [1], and is likely to increase in importance as other sources (e.g., jet noise) are further reduced. It is also certain to be an important issue in any forthcoming supersonic civil transport project. If the problem is to be tackled successfully, it must be addressed at the design stage, and there is thus a need for a simple model of the noise generation process, which can be used to formulate design criteria.

A model which fits this description, and which may be justified on the basis of the typical structural and boundary layer parameters of the problem [2], is a simply supported rectangular elastic plate driven by a flat-wall turbulent boundary layer. The sound power radiated by the plate may be calculated in terms of the cross-correlation function of the boundary layer fluctuation pressures, and an estimate of cabin noise levels then obtained by summing the incoming power contributions from all fuselage panels (plates). The model may also be extended to describe the modifying effects of the cabin interior wall treatment [3].

---

* Original version published in the proceedings of the First CEAS/AIAA Aeroacoustics Conference, Munich, Germany, 12–15 June 1995.

0022–460X/97/390541 + 25 $25.00/0/sv971114

The specific form in which the boundary layer pressure cross-correlation enters this model is the wavenumber–frequency spectrum, $\tilde{\Phi}_p(\mathbf{k}, \omega)$, obtained by Fourier transforming the correlation function in time and space. A number of more or less empirical expressions for this quantity are available, and it is the object of this work to determine the sensitivity of the model predictions for radiated sound to differences in these expressions, and thereby to assess their applicability to this and similar problems.

At this point, one should note that the formulation described here relies on the assumption that the pressure field on the flow side of the plate consists of the sum of the turbulence pressures which would be observed on a rigid wall and the acoustic pressures which would be generated by the plane motion in the absence of turbulence. This ‘‘weak coupling’’ approximation can be derived from an acoustic analogy analysis of the problem (examples of this approach may be found in references [4, 5]), subject to the condition that the acoustic velocities are small in comparison with the turbulence velocities. (Such a condition simply corresponds to the assumption implicit in acoustic analogy analyses; namely, that the basic turbulence structure is essentially unaffected by the acoustic motions.) The quantitative predictions that are obtained from the weak coupling approximation have been shown to work well in a wide range of cases [6–10], including supersonic flows [8, 9]. It has thus become accepted as a standard method, and is in widespread current use.

However, the assumption that the turbulence characteristics are unaffected by the acoustic field is sweeping, and is especially difficult to justify at supersonic flow speeds. Recently, Frendi [11] has presented calculations which avoid this problem, in that a fully coupled solution is sought for the turbulent flow and plate vibration. Current computational resources limit the flow model to an ‘‘unsteady Reynolds-averaged’’ (or ‘‘very large eddy simulation’’) formulation, but predictions are nonetheless obtained over a useful range of frequencies. This is clearly a valuable way forward, although it is not clear whether the errors associated with the weak coupling approximation justify the massively increased computational requirement. (Frendi [11] cites differences in plate damping between experimental and theoretical results presented by Wu and Maestrello [12] as evidence that these errors are large in supersonic flow; however, it is not clear to what extent the differences could have been due to difficulties in the modelling of structural damping. Certainly the results of references [8] and [9] show good agreement between supersonic flow experiments and predictions obtained with the weak coupling approximation, albeit not in very great detail.)

In any case, one is currently a long way from being able to apply fully coupled computations to problems of practical interest, such as the prediction of boundary layer induced cabin noise for complete aircraft [13]. Furthermore, even when it becomes feasible to do so, there will still be a requirement for simple models which enhance understanding and allow rapid computations to be performed at an early design stage. One can thus expect that the weak coupling approximation will remain in use for some considerable time yet; hence the importance of assessing the merits of the various models for the rigid wall pressure spectrum.

The paper commences with a description of the flat plate model and the results of the analysis for the radiated sound (section 2). The final expression takes the form of a sum of contributions from plate modes, and the physical interpretation of the components of each summand term is described, for both the bare and trimmed plate cases. Particularly important for this investigation is the modal excitation term, $\tilde{\Phi}_{mn}$, which represents the influence of the boundary layer wavenumber–frequency spectrum on the radiated sound, and this quantity is investigated further in section 3. Here the relationship between $\tilde{\Phi}_p(\mathbf{k}, \omega)$ and $\tilde{\Phi}_{mn}$ is discussed, and possible models for $\tilde{\Phi}_p(\mathbf{k}, \omega)$ are described. An initial

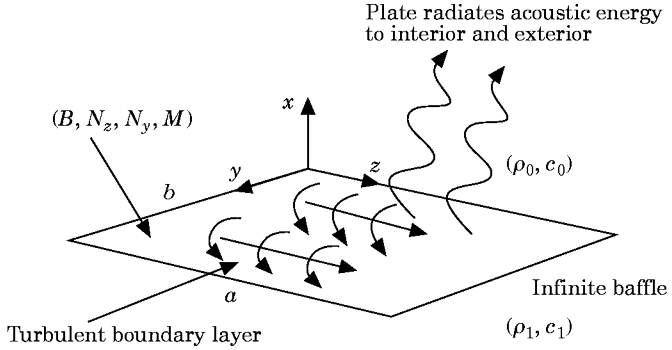

Figure 1. The flat plate model. A simply supported thin elastic plate, set in an infinite rigid baffle, is driven by a turbulent boundary layer. The resulting vibrations radiate acoustic energy to the interior ($x < 0$) and exterior ($x > 0$).

selection of promising candidates is made at this stage. In section 4 these formulations are then applied to two test cases, one representative of a high speed subsonic transport, and the other of a somewhat slower aircraft. The results are discussed and explained in terms of the characteristics of the candidate wavenumber–frequency spectrum models, and the conclusions of the investigation are then summarized in section 5.

2. THE BOUNDARY LAYER DRIVEN PLATE

2.1. GOVERNING EQUATIONS AND MODAL ANALYSIS

The basic model consists of a simply supported thin elastic plate, of length a and breadth b, set in an infinite rigid baffle and driven by a turbulent boundary layer (see Figure 1). The plate has bending stiffness B, membrane tensions N_y, N_z and mass per unit area M, and the bounding fluids are of density and sound speed ρ_0, c_0 and ρ_1, c_1 respectively. Under the weak coupling assumption, the driving pressures consist of the "blocked" (i.e., rigid wall) boundary layer pressure, p_t, and the acoustic pressure fluctuations induced by the plate motion. The harmonic plate velocity component $v(y, z, \omega)\,\mathrm{e}^{-\mathrm{i}\omega t}/2\pi$ then satisfies

$$B\nabla^4 v - N_z\,\partial^2 v/\partial z^2 - N_y\,\partial^2 v/\partial y^2 - M\omega^2 v = \mathrm{i}\omega[p_t + p_0 - p_1]_{x=0}, \qquad (2.1)$$

where $p_0\,(x, y, z, \omega)$ and $p_1\,(x, y, z, \omega)$ are the external and internal acoustic pressures. As such, they obey the Helmholtz equations*

$$(\nabla^2 + k_i^2)p_i = 0, \qquad i = 0,\ 1, \qquad (2.2)$$

(here k_i is the acoustic wavenumber, ω/c_i), and are linked to the plate velocity via the boundary conditions

$$(1/\rho_i)\,\partial p_i\,/\partial x|_{x=0} = \mathrm{i}\omega v, \qquad i = 0,\ 1, \qquad (2.3)$$

which specify equal plate and fluid displacements in the x direction. To complete the formulation of the problem, it remains only to include structural damping, which will be represented as a small imaginary component in the restoring force terms:

$$B = B_r\,(1 - \mathrm{i}\varepsilon_s), \qquad N_z = N_{zr}\,(1 - \mathrm{i}\varepsilon_s), \qquad N_y = N_{yr}\,(1 - \mathrm{i}\varepsilon_s). \qquad (2.4)$$

The quantity of interest is the spectrum of the inwardly radiated sound power, $S_1\,(\omega)$, defined by

---

* The influence of the flow on p_0 is neglected in equation (2.2).

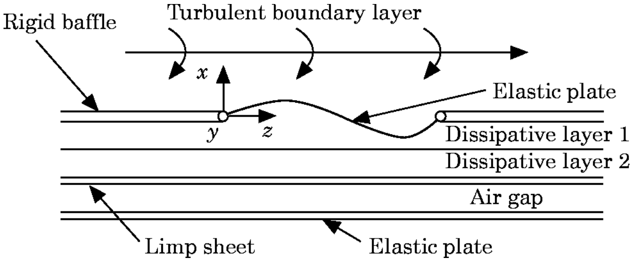

Figure 2. The trimmed flat plate model. The interior surface of the plate is now covered by a series of infinite layers, representing the interior treatment of a trimmed aircraft.

$$2\pi\delta(\omega-\omega')S_1(\omega) = -2\int_0^a\int_0^b \mathrm{Re}\,[\overline{p_1(0,y,z,\omega)v^*(y,z,\omega')}]\,\mathrm{d}y\,\mathrm{d}z. \tag{2.5}$$

The components of the integrand may be found from equations (2.1–2.3) via a modal analysis [2], and equation (2.5) then yields the dimensionless spectrum*

$$\tilde{S}_1(\omega) = \frac{M\omega^3}{U_c^2\,\Phi(\omega)}S_1(\omega) = 2\varepsilon_{f1}\sum_{m,n}\mathrm{Re}\,[Z_{mn}^{(1)}]\frac{\tilde{\Phi}_{mn}}{|d_{mn}|^2}, \tag{2.6}$$

where the terms have the following meanings: $\Phi(\omega)$ is the boundary layer pressure spectrum, U_c is the boundary layer eddy convection velocity, ε_{f1} is the fluid loading parameter ($=\rho_1 c_1/M\omega$), m and n are longitudinal and lateral mode numbers, $Z_{mn}^{(1)}$ is the dimensionless acoustic modal impedance, $\tilde{\Phi}_{mn}$ is the dimensionless modal excitation, and d_{mn} is the dimensionless overall modal impedance. Thus equation (2.6) expresses $\tilde{S}_1(\omega)$ as a sum of individual mode contributions, each contribution consisting of the modal energy, $\tilde{\Phi}_{mn}/|d_{mn}|^2$, multiplied by the "radiation efficiency", $\mathrm{Re}\,[Z_{mn}^{(1)}]$. Expressions for these terms are given in section 2.2, where their physical interpretations are discussed. (Note that the non-dimensionalization used here differs from that of reference [2] in employing $\Phi(\omega)$ instead of more fundamental boundary layer properties. This ensures that differences in $\tilde{S}_1(\omega)$ for the various wavenumber–frequency spectrum models will be entirely due to the feature one wishes to assess—the representation of the spatial correlation of the fluctuating pressures.)

The trimmed model, which includes a representation of the aircraft cabin interior treatment, is shown in Figure 2. Here the plate of Figure 1 is covered by two layers of dissipative material and a limp, massive sheet (representing an insulation bag), these in turn being separated from the internal air space by an air gap and an elastic plate (representing a trim panel). The modal analysis is similar to that for the bare plate, and yields [3]

$$\tilde{S}_1(\omega) = 2\varepsilon_{f1}\sum_{m,n}\mathrm{Re}\,[I_{mn}]\frac{\tilde{\Phi}_{mn}}{|d'_{mn}|^2}. \tag{2.7}$$

This equation is formally similar to equation (2.6), with $Z_{mn}^{(1)}$ replaced by I_{mn} and d_{mn} by d'_{mn}. The model's behaviour, however, is radically altered by the interior treatment, as described below.

---

* The expression given here is valid for light fluid-loading, when modal coupling due to the acoustic pressures is negligible [14].

2.2. PHYSICAL CHARACTERISTICS

Each summand term in equations (2.6) and (2.7) represents one of the three factors in the behaviour of the model problem—excitation, structural response and acoustic radiation. Here the terms will be considered in more detail, with equation (2.6) used as a basis for the discussion. The differences between equations (2.7) and (2.6) will be described where appropriate.

The acoustic modal impedance, $Z_{mn}^{(1)}$, is given by the integral

$$Z_{mn}^{(1)} = \frac{k_1}{(2\pi)^2} \int_{-\infty}^{\infty} \int_{-\infty}^{\infty} \frac{|S_{mn}(k_y, k_z)|^2}{(k_1^2 - k_y^2 - k_z^2)^{1/2}} \, \mathrm{d}k_y \, \mathrm{d}k_z, \tag{2.8}$$

where the square root is to be taken as positive real or positive imaginary, and the shape function $S_{mn}(k_y, k_z)$ is the spatial Fourier transform of the (m, n)th simply supported mode shape:

$$S_{mn}(k_y, k_z) = \frac{2}{\sqrt{ab}} \int_0^a \int_0^b \sin\left(\frac{m\pi z}{a}\right) \sin\left(\frac{n\pi y}{b}\right) \mathrm{e}^{-\mathrm{i}k_y y} \, \mathrm{e}^{-\mathrm{i}k_z z} \, \mathrm{d}y \, \mathrm{d}z. \tag{2.9}$$

The integral is easily evaluated, and $|S_{mn}(k_y, k_z)|^2$ is found to be given by a product of functions in k_y and k_z, peaking around the modal wavenumbers k_n $(=n\pi/b)$ and k_m $(=m\pi/a)$ respectively. To either side of the peak are an infinite number of side lobes, as shown in Figure 3. These functions represent the wavenumber content of the mode shape, which weights the acoustic impedance of each individual (k_y, k_z) Fourier component in equation (2.8) to give the acoustic modal impedance. The radiation efficiency is the real part of $Z_{mn}^{(1)}$, arising from the integration range $k_y^2 + k_z^2 \leqslant k_1^2$. Its magnitude thus depends on whether or not the shape function peak at the modal wavenumbers (k_m, k_n) lies in this range: i.e., on whether the mode is below $(k_m^2 + k_n^2 > k_1^2)$ or above $(k_m^2 + k_n^2 < k_1^2)$ coincidence. Below coincidence, the mode trace speed is subsonic and $\mathrm{Re}\,[Z_{mn}^{(1)}]$ is small; above coincidence the trace speed is supersonic and $\mathrm{Re}\,[Z_{mn}^{(1)}] \approx 1$. This behaviour may

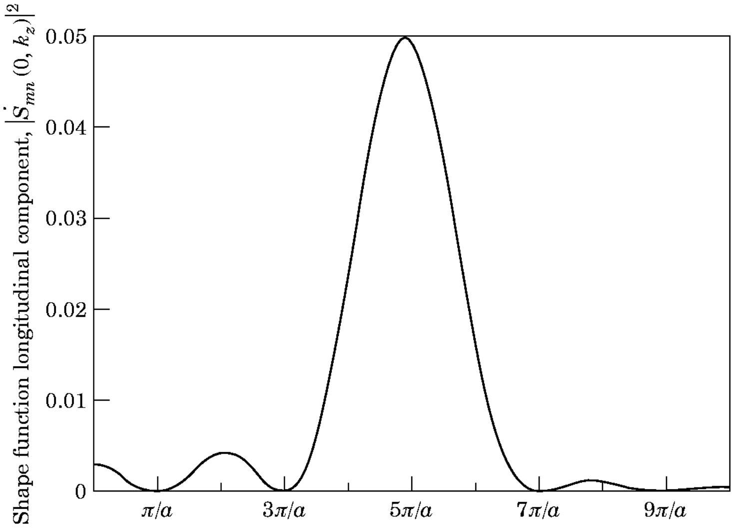

Figure 3. Shape function variation with longitudinal wavenumber for $m = 5$. The plot shows the squared magnitude of $S_{mn}(k_y, k_z)$ with $k_y = 0$. It is strongly peaked around the modal wavenumber, $k_z = m\pi/a$.

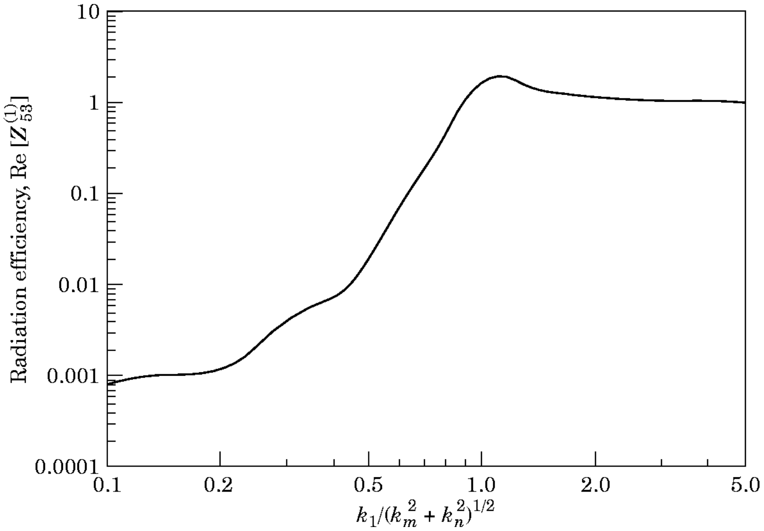

Figure 4. Mode (5,3) radiation efficiency for $a = 1$ m and $b = 0{\cdot}6$ m. The radiation efficiency is plotted against a dimensionless frequency, which is equal to one when the acoustic wavelength becomes equal to the modal wavelength. At lower frequencies the dominant modal wavenumber components are subsonic, and the radiation efficiency is low. At higher frequencies, the radiation efficiency asymptotes to one.

clearly be seen in Figure 4, which shows a typical example. One may thus divide modes into two classes, "inefficient" and "efficient", corresponding to below and above coincidence.

The corresponding term for the trimmed plate, $\mathrm{Re}\,(I_{mn})$, similarly represents the radiation efficiency of mode (m, n), but differs significantly from $\mathrm{Re}\,[Z_{mn}^{(1)}]$, due to the attenuating effect of the insulation and trim, which increases with frequency [3]. However, at any given frequency, an above-coincidence mode still has a much higher supersonic wavenumber content than one below coincidence, and the concepts of efficient and inefficient modes still apply.

The second term in equation (2.6), d_{mn}, describes the structural response. It is given by

$$d_{mn} = \mathrm{i}\left\{\frac{B(k_m^2 + k_n^2)^2 + N_z\,k_m^2 + N_y\,k_n^2}{M\omega^2} - 1\right\} + \varepsilon_{f0}\,Z_{mn}^{(0)} + \varepsilon_{f1}\,Z_{mn}^{(1)}, \tag{2.10}$$

where ε_{f0} and $Z_{mn}^{(0)}$ are the external equivalents of ε_{f1} and $Z_{mn}^{(1)}$. At the modal resonance frequency, $\mathrm{Im}\,(d_{mn}) = 0$, and the mode's response is limited only by the (small) real part of d_{mn}, which arises from the structural damping terms of equation (2.4) and the external and internal modal radiation efficiencies.

For the trimmed plate, d'_{mn} is formed by replacing the term $\varepsilon_{f1}\,Z_{mn}^{(1)}$ with one representing the modal impedance of the insulation/trim/internal air system, $\varepsilon_{fi}\,Z_{mn}^{(i)}$. In contrast to the former, $\varepsilon_{fi}\,Z_{mn}^{(i)}$ can have a significant real part even for inefficient modes, due to the dissipative nature of the insulation, and the effect is greatly to increase the apparent damping of the plate [3].

Finally, the excitation term $\tilde{\Phi}_{mn}$ is, like $Z_{mn}^{(1)}$, given by a wavenumber integral,

$$\tilde{\Phi}_{mn} = \frac{1}{(2\pi)^2}\int_{-\infty}^{\infty}\int_{-\infty}^{\infty} \tilde{\Phi}_p\,(k_y, k_z, \omega)\,|S_{mn}\,(k_y, k_z)|^2\,\mathrm{d}k_y\,\mathrm{d}k_z, \tag{2.11}$$

where $\tilde{\Phi}_p\,(k_y, k_z, \omega)$ is the dimensionless wavenumber–frequency spectrum of the boundary layer pressures, defined by

$$2\pi\delta(\omega-\omega')\tilde{\Phi}_p\,(k_y, k_z, \omega)$$

$$=\frac{\omega^2}{U_c^2\,\Phi(\omega)}\int_{-\infty}^{\infty}\int_{-\infty}^{\infty}\overline{p_t\,(0, y+r_y, z+r_z, \omega)p_t^*\,(0, y, z, \omega')}\,\mathrm{e}^{-\mathrm{i}k_y r_y}\,\mathrm{e}^{-\mathrm{i}k_z r_z}\,\mathrm{d}r_y\,\mathrm{d}r_z. \tag{2.12}$$

Most of the energy in the boundary layer pressure fluctuations lies around the wavenumbers $k_z=\omega/U_c, k_y=0$*, so that $\tilde{\Phi}_p\,(\mathbf{k}, \omega)$ is strongly peaked there. The modes undergoing the highest excitation are thus those with modal wavenumbers (k_m, k_n) close to $k_z=\omega/U_c$, $k_y=0$, when the shape function and wavenumber–frequency spectrum peaks coincide.

The extent of a given mode's contribution to the radiated sound is thus dependent on whether it is acoustically efficient or inefficient, whether it is resonant or non-resonant, and whether or not it is highly excited. Of particular interest are modes which combine two of these properties, either acoustic efficiency and resonance, or high excitation and resonance (“hydrodynamic coincidence”). (The third possibility, high excitation and acoustic efficiency, is not possible for subsonic boundary layers.) For resonant modes to be acoustically efficient, the frequency must be above the “coincidence” or “critical” frequency, at which the free wave speed in the corresponding infinite plate becomes supersonic. By contrast, hydrodynamic coincidence may occur at any frequency, and simply requires the boundary layer convection velocity U_c to match the longitudinal trace speed ω/k_m of a resonant mode, the effect being most pronounced for modes with k_n small.

Clearly, given the above discussion, it is not possible to determine *a priori* which modes will dominate the radiated power spectrum. This is a significant limitation, because it affects the choice of model for the boundary layer wavenumber–frequency spectrum, as will become evident in the following assessment of possible candidates.

3. THE MODAL EXCITATION TERM

3.1. GENERAL FEATURES OF THE INTEGRAL

In discussing the integral for $\tilde{\Phi}_{mn}$, equation (2.11), and how it is affected by the choice of model for $\tilde{\Phi}_p\,(\mathbf{k}, \omega)$, one must first consider which regions of the integrand contribute most to it. This is clear for highly excited modes, where the peaks in the modal and boundary layer wavenumber spectra coincide. However, one also potentially needs to know where the main contributions to $\tilde{\Phi}_{mn}$ arise for weakly excited modes. In this case the integrand functions may typically be as shown in Figure 5, and one must consider which peak gives the larger contribution. In addressing this problem, Hwang and Maidanik [15] concluded that, for simply supported modes, it is the modal peak, which implies that it is necessary to know $\tilde{\Phi}_p\,(\mathbf{k}, \omega)$ accurately away from the convective peak. Thus, in the following discussion of possible models for $\tilde{\Phi}_p\,(\mathbf{k}, \omega)$, one of the features of interest will be their behaviour here.

---

* If the boundary layer were a perfectly frozen eddy pattern convecting at speed U_c, all of the energy would be concentrated here.

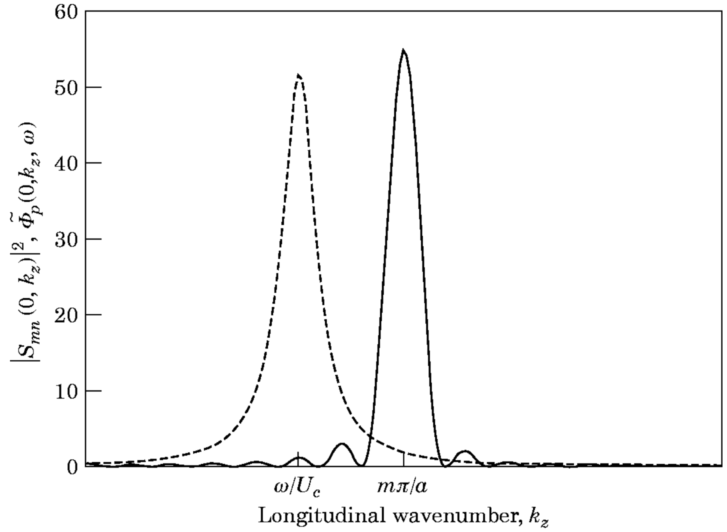

Figure 5. Components of the modal excitation integral. ——, Shape function; - - - -, wavenumber–frequency spectrum. The shape function peaks at $k_z = m\pi/a$, the wavenumber–frequency spectrum at $k_z = \omega/U_c$.

3.2. WAVENUMBER–FREQUENCY SPECTRUM MODELS

3.2.1. *Introduction*

Of early models for $\tilde{\Phi}_p(\mathbf{k}, \omega)$, the spatial Fourier transform of Corcos' curve fit to measured narrow-band pressure correlations [16] quickly established itself. However, experimental evidence suggesting that the Corcos model overpredicts levels at wavenumbers below the convective peak began to accumulate [17], and later workers, notably Chase [18, 19] and Ffowcs Williams [20] used analytical or quasi-analytical approaches in attempts to describe this region more accurately. More recently, refined versions of the Corcos approach have also appeared [21, 22]. The six models described in these references will form the basis for this investigation, and a brief description of each follows.

3.2.2. *The Corcos model*

Corcos' curve-fit for the narrow-band spatial correlation between wall pressures separated by (r_y, r_z) in (y, z) is [16]

$$\Phi_p(r_y, r_z, \omega) = \Phi(\omega)\, e^{-\alpha_y|\omega r_y|/U_c}\, e^{-\alpha_z|\omega r_z|/U_c}\, e^{i\omega r_z/U_c}, \tag{3.1}$$

where α_y and α_z are parameters chosen to yield the best agreement with experiment. After Fourier transforming in r_y, r_z, one finds [2, 17]

$$\tilde{\Phi}_p(\mathbf{k}, \omega) = 4\alpha_y\,\alpha_z/[\alpha_y^2 + U_c^2 k_y^2/\omega^2]\,[\alpha_z^2 + (U_c k_z/\omega - 1)^2]. \tag{3.2}$$

Various values for α_y and α_z are given in the literature; here $\alpha_y = 0{\cdot}77$ and $\alpha_z = 0{\cdot}1$ are used, in contradiction to Blake's recommended values ($\alpha_y = 0{\cdot}7$, $\alpha_z = 0{\cdot}32$) for aircraft boundary layers [17]. The reasons for this choice are discussed below.

3.2.3. *The Efimtsov model*

The Efimtsov model [21] follows the Corcos philosophy, but takes into account the dependence of spatial correlation on boundary layer thickness, δ, as well as spatial separation. Thus the correlation lengths $\Lambda_y\ (=U_c/|\omega|\alpha_y)$ and $\Lambda_z\ (=U_c/|\omega|\alpha_z)$ are given by the empirical expressions

$$\frac{\Lambda_z}{\delta}=\left[\left(\frac{a_1\,Sh}{U_c/u_\tau}\right)^2+\frac{a_2^2}{Sh^2+(a_2/a_3)^2}\right]^{-1/2}, \tag{3.3}$$

$$\frac{\Lambda_y}{\delta}=\left[\left(\frac{a_4\,Sh}{U_c/u_\tau}\right)^2+\frac{a_5^2}{Sh^2+(a_5/a_6)^2}\right]^{-1/2}, \qquad M_\infty<0{\cdot}75, \tag{3.4a}$$

$$\frac{\Lambda_y}{\delta}=\left[\left(\frac{a_4\,Sh}{U_c/u_\tau}\right)^2+a_7^2\right]^{-1/2}, \qquad M_\infty>0{\cdot}9, \tag{3.4b}$$

where M_∞ is the free-stream Mach number, and $Sh=\omega\delta/u_\tau$, with u_τ the friction velocity.* The constants a_1–a_7 are, respectively, 0·1, 72·8, 1·54, 0·77, 548, 13·5 and 5·66. Values for Λ_y when $0{\cdot}75<M_\infty<0{\cdot}9$ are not given; here interpolation is used if necessary.

Thus, at high frequencies these expressions correspond to a Corcos model with $\alpha_y=0{\cdot}77$ and $\alpha_z=0{\cdot}1$, the values chosen above. Since Efimtsov's results are derived from an extensive series of measurements on aircraft, over a Mach number range 0·41–2·1, they have been taken in preference to Blake's recommendations, which are based on a much more limited data set reported by Bhat [23]. Bhat found lower correlation lengths than those corresponding to the (smooth wall) parameters $\alpha_y=0{\cdot}77$ and $\alpha_z=0{\cdot}1$, and suggested that this was partially due to misalignment between the z-axis and the flow direction, and partially to surface roughness; hence Blake's choice of the rough-wall value $\alpha_z=0{\cdot}32$. However, the discrepancy with Efimtsov's results could be entirely accounted for by flow misalignment and another effect not considered: the drop in correlation lengths with Sh, which would affect the lower frequencies in Bhat's data set. Efimtsov's expressions must therefore be accepted as more reliable.

The corresponding wavenumber–frequency spectrum is obtained by replacing α_y and α_z in equation (3.2) by $U_c/|\omega|\Lambda_y$ and $U_c/|\omega|\Lambda_z$ respectively. Thus, although this model represents an improvement on that of Corcos, it still suffers from the same tendency to overpredict the spectrum at low wavenumbers.

3.2.4. *The Smol'yakov and Tkachenko model*

Like Efimtsov, Smol'yakov and Tkachenko [22] measured spatial pressure correlations as a function of spatial separation and boundary layer thickness, and fitted exponential curves to their results. However, rather than directly multiplying their expressions for pure lateral and pure longitudinal separation, giving an exponential with argument $-(|r_y|/\Lambda_y+|r_z|/\Lambda_z)$, they took the combined correlation to be of the form $\exp[-(r_y^2/\Lambda_y^2+r_z^2/\Lambda_z^2)^{1/2}]$, and Fourier transformed this expression. The resulting low wavenumber levels are an improvement on the Corcos prediction, but are still higher than experimental values, so a correction was added to the model to bring it into agreement without significantly affecting the convective peak levels. The final expression is

$$\tilde{\Phi}_p(\mathbf{k},\omega)=0{\cdot}974A(\omega)h(\omega)\,[F(\mathbf{k},\omega)-\Delta F(\mathbf{k},\omega)], \tag{3.5}$$

---

* In terms of the skin-friction coefficient c_f, and free-stream velocity U_∞, $u_\tau=U_\infty\sqrt{c_f/2}$.

with

$$A(\omega) = 0{\cdot}124\left[1 - \frac{U_c}{4\omega\delta^*} + \left(\frac{U_c}{4\omega\delta^*}\right)^2\right]^{1/2}, \qquad h(\omega) = \left[1 - \frac{m_1 A}{6{\cdot}515\sqrt{G}}\right]^{-1}, \tag{3.6, 3.7}$$

$$m_1 = \frac{1 + A^2}{1{\cdot}025 + A^2}, \qquad G = 1 + A^2 - 1{\cdot}005 m_1, \tag{3.8}$$

$$F(\mathbf{k}, \omega) = \left[A^2 + \left(1 - \frac{k_z U_c}{\omega}\right)^2 + \left(\frac{k_y U_c}{6{\cdot}45\omega}\right)^2\right]^{-3/2}, \tag{3.9}$$

$$\Delta F(\mathbf{k}, \omega) = 0{\cdot}995\left[1 + A^2 + \frac{1{\cdot}005}{m_1}\left\{\left(m_1 - \frac{k_z U_c}{\omega}\right)^2 + \left(\frac{k_y U_c}{\omega}\right)^2 - m_1^2\right\}\right]^{-3/2}. \tag{3.10}$$

(Here δ^* is the boundary layer displacement thickness, and is taken to be $\delta/8$.)

3.2.5. *The Ffowcs Williams model*

Starting from Lighthill's acoustic analogy, and assuming that the velocity source terms were of the general Corcos form, Ffowcs Williams [20] derived an expression for $\tilde{\Phi}_p(\mathbf{k}, \omega)$ containing several unknown constants and functions, to be determined experimentally. To date, these remain unknown, but Hwang and Geib [24] have proposed a simplified version, in which they neglect the effects of compressibility and assume a specific form for the remaining functions; their expression, slightly adjusted to agree with the Corcos parameters used here, is

$$\tilde{\Phi}_p(\mathbf{k}, \omega) = \left(\frac{U_c|\mathbf{k}|}{\omega}\right)^2 \frac{4\alpha_y \alpha_z}{[\alpha_y^2 + U_c^2 k_y^2/\omega^2][\alpha_z^2 + (U_c k_z/\omega - 1)^2]}. \tag{3.11}$$

3.2.6. *The Chase models*

From essentially the same starting point as Ffowcs Williams, but employing a number of heuristic arguments in his derivation, Chase [18] formulated a more specific model, containing a number of adjustable constants. His expression is

$$\frac{\tilde{\Phi}_p(\mathbf{k}, \omega)}{(2\pi)^3} = \frac{\rho^2\omega^2 u_\tau^3}{U_c^2\,\Phi(\omega)}\left(\frac{C_M k_z^2}{[K_+^2 + (b_M\delta)^{-2}]^{5/2}} + \frac{C_T|\mathbf{k}|^2}{[K_+^2 + (b_T\delta)^{-2}]^{5/2}}\right), \tag{3.12}$$

with

$$K_+^2 = \frac{(\omega - U_c k_z)^2}{h^2 u_\tau^2} + |\mathbf{k}|^2, \qquad \frac{\Phi(\omega)}{2\pi} = \frac{2\pi h \rho^2 u_\tau^4}{3\omega(1 + \mu^2)}(C_M F_M + C_T F_T), \tag{3.13, 3.14}$$

$$F_M = [1 + \mu^2\alpha_M^2 + \mu^4(\alpha_M^2 - 1)]/[\alpha_M^2 + \mu^2(\alpha_M^2 - 1)]^{3/2}, \tag{3.15}$$

$$F_T = [1 + \alpha_T^2 + \mu^2(3\alpha_T^2 - 1) + 2\mu^4(\alpha_T^2 - 1)]/[\alpha_T^2 + \mu^2(\alpha_T^2 - 1)]^{3/2}, \tag{3.16}$$

$$\alpha_{M\text{ or }T}^2 = 1 + (U_c/b_{M\text{ or }T}\,\omega\delta)^2, \qquad \mu = h u_\tau/U_c, \tag{3.17}$$

and, based on Chase's recommendations, the constants have values $C_M = 0{\cdot}0745$, $C_T = 0{\cdot}0475$, $b_M = 0{\cdot}756$, $b_T = 0{\cdot}378$ and $h = 3{\cdot}0$. (In fact, Chase's comparisons were performed allowing h to vary somewhat, with μ kept constant, but here later workers [17, 24] are followed in keeping to the spirit of the model and holding h constant. Also neglected is the difference between Chase's source convection velocity and U_c, the measured pressure convection velocity, and the expressions defining $\Phi(\omega)$ differ from Chase's in being exact. These alterations make little difference to the model's predictions.)

This model suffers from two deficiencies: it takes no account of the supersonic region ($|k_z| < \omega/c_0$) and it does not reproduce the approximately "wavenumber white" characteristics of experimental observations in the low wavenumber ($\omega/c_0 < k_z \ll \omega/U_c$) region [17]. In an attempt to remedy these problems, Chase [19] relaxed the requirement for a low wavenumber dependence $\sim |\mathbf{k}|^2$ (the Kraichnan–Phillips theorem) and included terms describing the acoustic region. Unfortunately, however, the constants multiplying the latter factors are not known and, like the Ffowcs Williams model, this formula can be used only in a limited form, without the terms describing the supersonic region. In this case, the result is

$$\tilde{\Phi}_p(\mathbf{k}, \omega)/(2\pi)^3 = \frac{\rho^2\omega^2 u_\tau^3}{U_c^2\,\Phi(\omega)\,[K_+^2 + (b\delta)^{-2}]^{5/2}}\left(C_M k_z^2 + C_T |\mathbf{k}|^2 \frac{K_+^2 + (b\delta)^{-2}}{|\mathbf{k}|^2 + (b\delta)^{-2}}\right), \quad (3.18)$$

with

$$\Phi(\omega)/2\pi = [2\pi h \rho^2 u_\tau^4/3\omega(1 + \mu^2)]\,(C_M F_M + C_T F_T), \quad (3.19)$$

$$F_M = [1 + \mu^2\alpha^2 + \mu^4(\alpha^2 - 1)]/[\alpha^2 + \mu^2(\alpha^2 - 1)]^{3/2}, \quad (3.20)$$

$$F_T = \tfrac{3}{2}(1 + \mu^2)(1 + \alpha^2)/\alpha^3. \quad (3.21)$$

Here the term F_M is still exact, but F_T is Chase's approximate result. The recommended constants are $h = 3{\cdot}0$, $hC_M = 0{\cdot}466$, $hC_T = 0{\cdot}014$ and $b = 0{\cdot}75$.

3.3. PRELIMINARY MODEL ASSESSMENT

Before returning to the modal excitation term, $\tilde{\Phi}_{mn}$, and how it is influenced by the choice of model, it will be helpful first to consider the expressions for the wavenumber–frequency spectrum in isolation. In Figure 6 are shown the predictions for the variation of $\tilde{\Phi}_p(\mathbf{k}, \omega)$

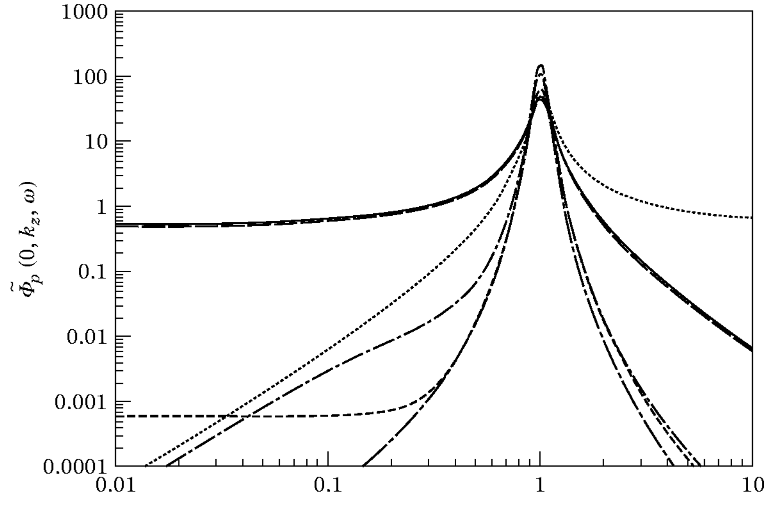

Figure 6. Wavenumber–frequency spectra for $Sh = 248$. ——, Corcos; — —, Efimtsov; - - - Smol'yakov and Tkachenko; · · · · ·, Ffowes Williams; —·—·, Chase I; –·–·, Chase II. The spectra are plotted against longitudinal wavenumber non-dimensionalized on the convective wavenumber ω/U_c, and thus peak around one.

with dimensionless longitudinal wavenumber $U_c k_z/\omega$, for $Sh = 248$. At this frequency, the Corcos and Efimtsov models coincide, and their curves virtually overlie one another, predicting levels comparable to the other models at the convective peak, but significantly higher at lower wavenumbers.

The effect of the Smol'yakov and Tkachenko novel formulation for combining the effects of longitudinal and lateral spatial separation is seen in the narrower convective peak associated with their model, and in the smaller low wavenumber levels, although the latter difference is also due to the correction function ΔF. Somewhat comparable low wavenumber behaviour is shown by the second Chase model; the first, like the Ffowcs Williams model, demonstrates the effect of being required to exhibit a $|\mathbf{k}|^2$ dependence at low wavenumbers.

At lower frequencies, the influence of boundary layer thickness becomes important, and Figure 7 (for $Sh = 24{\cdot}8$) shows how this affects the various models. The Corcos spectrum, which takes no account of δ, is unchanged, but now the Efimtsov convective peak is significantly broader, due to its much smaller correlation lengths. Smol'yakov and Tkachenko also have correlation lengths limited by boundary layer thickness, but predict intermediate values, so their peak is less affected by broadening. Little difference in the peaks of the other models is visible, but the second Chase model now shows no signs whatsoever of a "wavenumber white" region—it is, in fact, observed only for $(b\delta)^{-1} \ll k_z \ll \omega/U_c$, a range which is not distinct at lower frequencies.

At this stage, the models under consideration are reduced to Corcos, Efimtsov, Smol'yakov and Tkachenko, and Chase I. The Hwang and Geib interpretation of the Ffowcs Williams model is rejected because it does not satisfy the integral requirement

$$\frac{1}{(2\pi)^2}\int_{-\infty}^{\infty}\int_{-\infty}^{\infty} \tilde{\Phi}_p\,(k_y, k_z, \omega)\left(\frac{U_c}{\omega}\right)^2 \mathrm{d}k_y\,\mathrm{d}k_z = 1. \tag{3.22}$$

In fact, for the expression given in equation (3.11), the integral is divergent, as one would expect from the high wavenumber behaviour observed in Figures 6 and 7. In any case,

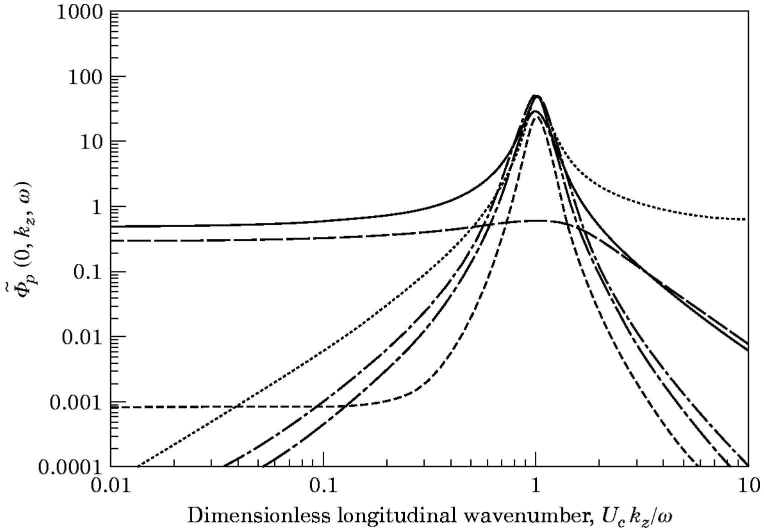

Figure 7. Wavenumber–frequency spectra for $Sh = 24{\cdot}8$. ——, Corcos; — —, Efimtsov; - - - - Smol'yakov and Tkachenko; · · · ·, Ffowes Williams; —·—·, Chase I; –·–·, Chase II.

the low wavenumber behaviour of this model is mirrored by the first Chase model, so that one will still be able to assess the effect of a $|\mathbf{k}|^2$ dependence in $\tilde{\Phi}_p(\mathbf{k}, \omega)$ in the subconvective region.

A similar argument applies to Chase II, since the Smol'yakov and Tkachenko model gives a better representation of a flat spectrum at low wavenumber. Additionally, though, the peak levels predicted in Figures 6 and 7 are significantly above those of other models, leading one to suspect that Chase's approximation to $\Phi(\omega)$, equation (3.19), may not be wholly accurate and hence that this model too would not satisfy condition (3.22). This assertion tends to be confirmed when the calculations presented in section 4 are repeated with Chase II.

3.4. NUMERICAL EVALUATION OF THE $\tilde{\Phi}_{mn}$ INTEGRAL

In general, analytical solutions of equation (2.11) are not available. The integral must therefore be evaluated numerically, and this is achieved by using Gaussian quadrature. At frequencies where the convective peak in $\tilde{\Phi}_p(\mathbf{k}, \omega)$ is broad in comparison to the lobes in $|S_{mn}(k_y, k_z)|^2$, the integral can be performed lobe-by-lobe, with the lobe shape taken as a weighting function. Otherwise, a uniform Gaussian quadrature is employed either side of the convective peak. Analytical expressions for the integral of the shape function term are used to provide upper bounds on the truncation error for the integrals, which is required to be less than 0·5%. The numerical results have been checked with analytical expressions derived for the Corcos model [2], and found to agree closely, with an overall accuracy typically better than 0·5%.

4. THE RADIATED SOUND POWER

4.1. TEST CASES

In this section, the effect of the choice of wavenumber–frequency spectrum model on the predicted sound radiation from the plate, with and without insulation and trim, is investigated for the frequency range typically of interest for boundary layer noise, 500–5000 Hz [1]. Two test cases are considered, (a) and (b), the former being representative of a high-speed subsonic aircraft, and the latter of a lower speed vehicle. Parameters for case (a) are as follows: free-stream velocity U_∞, 240 m s^{-1}; skin friction coefficient c_f, 0·002; boundary layer thickness δ, 0·06 m; plate mass/unit area M, 2·77 kg m^{-2}; plate bending stiffness B_r, 6·0 Nm; plate longitudinal tension N_{zr}, 29300 N m^{-1}; plate lateral tension N_{yr}, 62100 N m^{-1}; structural damping factor ε_s, 0·02; plate length a, 0·5 m; plate width b, 0·2 m; external air density ρ_0, 0·44 kg m^{-3}; external sound speed c_0, 300 m s^{-1}; internal air density ρ_1, 1·2 kg m^{-3}; internal sound speed c_1, 340 m s^{-1}.

At this stage, it is instructive to consider which class of modes is likely to contribute most to the radiated sound in case (a). Since the excitation is subsonic, there can be no efficient, resonant and highly excited modes, but efficient and resonant, or highly excited and resonant modes are possible. For the parameters cited, however, the critical frequency is around 10 kHz, which obviates the first possibility. The second depends on whether hydrodynamic coincidence occurs, and to determine this one needs to know the boundary layer convection velocity U_c, and the modal resonance frequencies. The latter are shown in Figure 8(a), where resonance frequency is plotted against mode number m for modes with $n = 1, \ldots, 4$. Also plotted are the lines corresponding to $k_m = \omega/U_c$ for $U_c = 0{\cdot}75U_\infty$

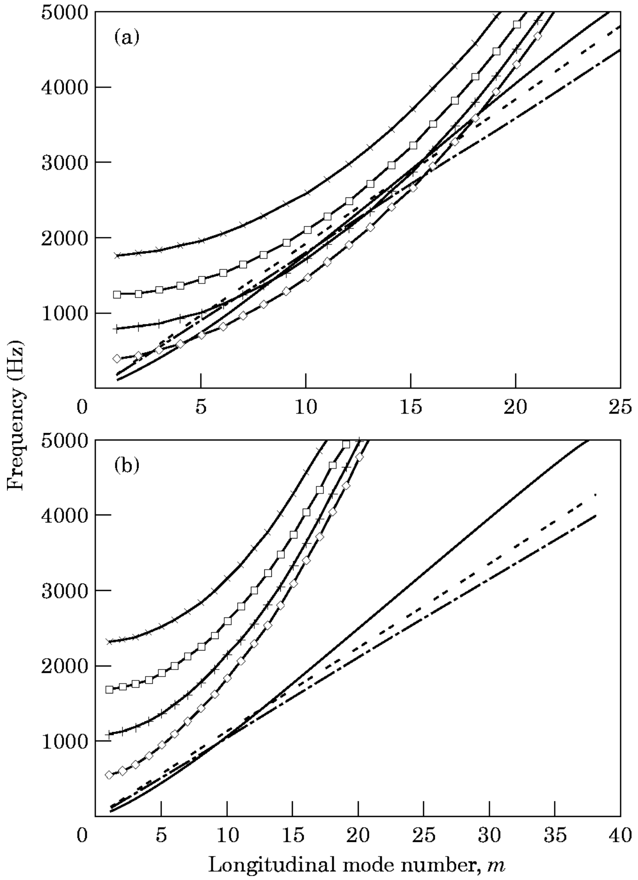

Figure 8. Resonance frequencies and convective peak locations. (a) Case (a); (b) case (b). Resonance frequencies (plotted against the longitudinal mode number m). —◇—, $n=1$; —|—, $n=2$; —□—, $n=3$; —×— $n=4$. Convective peak frequencies (defined by $\omega/U_c = m\pi/a$): ——, U_c from equation (4.1); —·—·-, $U_c = 0{\cdot}75\,U_\infty$; - - - -, $U_c = 0{\cdot}8\,U_\infty$.

(the value recommended by Chase for his first model), $U_c = 0{\cdot}8U_\infty$ (the Smol'yakov and Tkachenko figure) and

$$\frac{U_c}{u_\tau} = 9{\cdot}55Sh^{1/5}\left[\frac{1 + (6{\cdot}38 \times 10^{-4}Sh)^2}{1 + (3{\cdot}98 \times 10^{-3}Sh)^4}\right]^{1/10}, \tag{4.1}$$

which is the empirical fit obtained by Efimtsov. Hydrodynamic coincidence is evident over the majority of the frequency range, with the convective peak at or close to the modal wavenumbers of the resonant modes for frequencies between 500 Hz and 4000 Hz. In this case, then, one may expect highly excited, resonant, inefficient modes to dominate the radiated sound, in preference to the weakly driven, non-resonant efficient modes. If this is so, then the influence of the wavenumber–frequency spectrum model should be confined to its description of the convective peak.

Less clear is what would happen if there were no hydrodynamic coincidence over the frequency range. To investigate this possibility, one can consider case (b), where the free-stream velocity is reduced to 140 m s^{-1} and, to emphasize the difference, the plate is stiffened by doubling the in-plane tensions. The Sh range is kept unchanged by taking $\delta = 0{\cdot}04$ and $c_f = 0{\cdot}0025$. The resonance frequencies and convective peak positions for these parameters are plotted in Figure 8(b), showing that the resonant mode wavenumbers now lie in the low wavenumber region of $\tilde{\Phi}_p$ (**k**, ω). In this case, either the highly excited modes, or the resonant modes, or the efficient modes might give the largest contribution to the radiated sound, and one cannot predict which range of $\tilde{\Phi}_p$ (**k**, ω) is likely to be most important.

In order to isolate the influence of wavenumber–frequency spectrum shape in the test cases, the comparison between models will use the same convection velocity for all; this being given by equation (4.1). However, as there is some disagreement on this point, results from the Chase I and Smol'yakov and Tkachenko models with their recommended constant values are also compared. All the results presented were obtained by using the numerical approach to evaluating $\tilde{\Phi}_{mn}$ described in section 3.4; other details of the calculation method, in particular the evaluation of the modal radiation efficiency, may be found in references [2–4].

4.2. TEST CASE (A)

4.2.1 *Model comparisons*

To confirm the expectation that the hydrodynamic coincidence modes will dominate the radiated sound in this case, the contributions from four mode classes are considered: namely, in order of decreasing wavelength, class 1 (efficient, above coincidence), class 2 (below coincidence, mass-limited), class 3 (below coincidence, resonant) and class 4 (below coincidence, stiffness-limited). A below coincidence mode is deemed mass- or stiffness-limited if its *in vacuo* vibration energy would be predicted to within 1% with the structural damping term removed from d_{mn}. The contributions from these classes to the radiated sound, with the Efimtsov model for $\tilde{\Phi}_p$ (**k**, ω), are shown in Figure 9, where it is evident that the only significant contribution comes from resonant modes. As the Efimtsov model has the highest low wavenumber spectrum levels relative to the convective peak, this conclusion will also hold for the other wavenumber–frequency spectrum models.

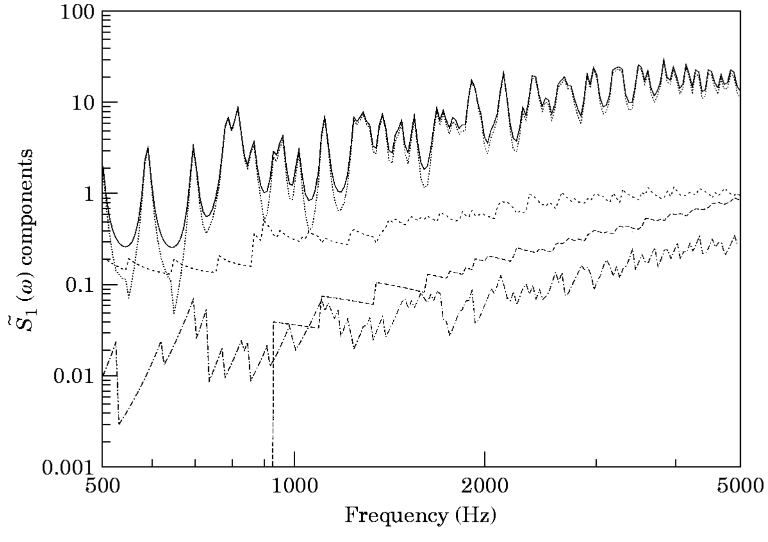

Figure 9. Radiated power spectrum by mode class for case (a), obtained by using the Efimtsov model. ——, Overall power; – –, efficient modes; - - - -, mass-limited modes; · · · ·, resonant modes; – · – ·, stiffness-limited modes. The resonant mode contribution dominates over the entire frequency range.

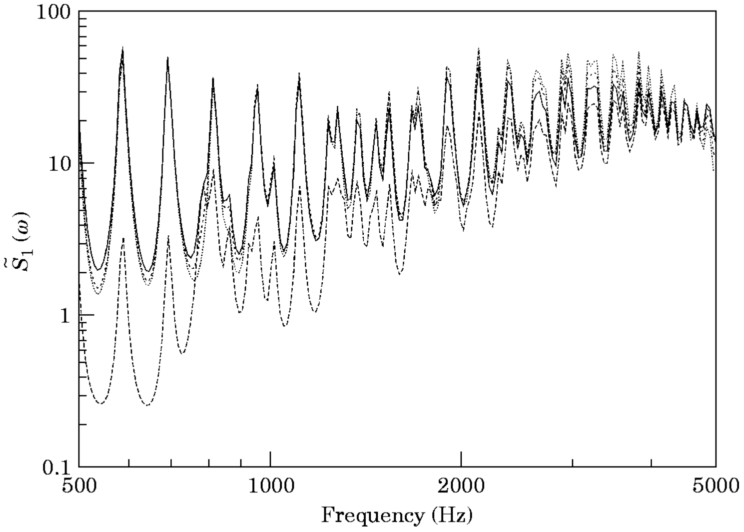

Figure 10. Radiated power spectra for case (a). ——, Corcos; – –, Efimtsov; - - - -, Smol'yakov and Tkachenko; · · · ·, Chase I.

may thus now confine attention to the overall radiated power, plotted in Figure 10 for the four models under consideration. At low frequencies the predictions of the Corcos, Smol'yakov and Tkachenko and Chase I models are strikingly consistent, while that of the Efimtsov model is significantly lower. The latter approaches the Corcos curve with increasing frequency, while the Smol'yakov and Tkachenko and Chase I plots first rise above it, and then finally drop below.

In discussing these observations, one can note first that the spectrum plots of Figures 6 and 7 correspond to conditions at 5000 Hz and 500 Hz respectively. Thus the Efimtsov prediction should indeed tend towards Corcos with increasing frequency, and is lower because its convective peak levels are lower. However, the detailed shape of the other three models' convective peaks is irrelevant to the sound radiation at low frequencies, because here they are sufficiently narrow in comparison to the lobes of $|S_{mn}(k_y, k_z)|^2$ (see Figure 5) to behave essentially like delta functions, picking out the value of the shape function magnitude at $k_z = \omega/U_c$. At higher frequencies, though, the situation tends to reverse, the shape function lobes becoming narrow in comparison to the convective peak, and here the details of the latter's shape start to become important. Thus, when the main peak in $|S_{mn}(k_y, k_z)|^2$ lies close to ω/U_c, the higher levels at the convective peak lead to larger predictions from Smol'yakov and Tkachenko and Chase I, while at the highest frequencies the modal wavenumbers have moved sufficiently far away for $|S_{mn}(k_y, k_z)|^2$ to be picking out larger values from the Corcos model. This is significant, as it implies that the choice of model for $\tilde{\Phi}_p(\mathbf{k}, \omega)$ is important even if the crucial region is the convective peak, rather than the low wavenumber regime. In particular, the form of spatial correlation assumed in the empirical models may be influential, and this issue will be returned to in section 4.2.3.

The effect of the choice of U_c on the Smol'yakov and Tkachenko and Chase I models is shown in Figures 11 and 12, where significant differences in spectrum levels are evident. At low frequencies, the constant convection velocities are higher than Efimtsov's value, moving the narrow convective peaks away from the maximum value of $|S_{mn}(k_y, k_z)|^2$ and reducing the predicted radiation. The broadening of the convective peak with increasing frequency and the convergence of the convection velocities in the mid-frequency range

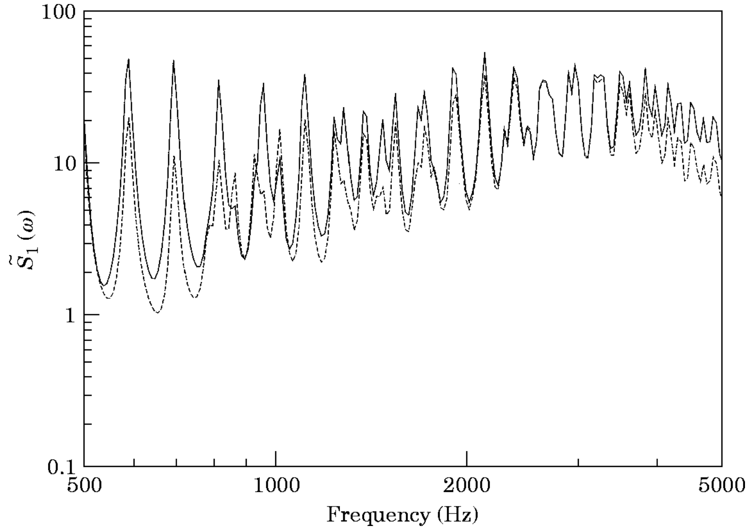

Figure 11. Case (a): sensitivity of the Smol'yakov and Tkachenko radiated power prediction to the choice of convection velocity: ——, U_c from equation (4.1); - - - -, $U_c = 0{\cdot}8U_\infty$.

leads to a merging of spectrum levels, but above about 4 kHz the resonant modes find themselves further into the low wavenumber region of $\tilde{\Phi}_p(\mathbf{k}, \omega)$ for the fixed convection velocities, and the predictions again diverge.

4.2.2. *Influence of cabin trim*

In the case of the trimmed plate, with the parameters given in reference [3], the increased effective structural damping takes out the sharp peaks in the resonant mode response, and the sound attenuation in the insulation drops both efficient and resonant mode radiation efficiencies by about the same factor. From Figure 9 then, one can see that the resonant modes will remain the dominant contributors to the radiated sound, and this is confirmed

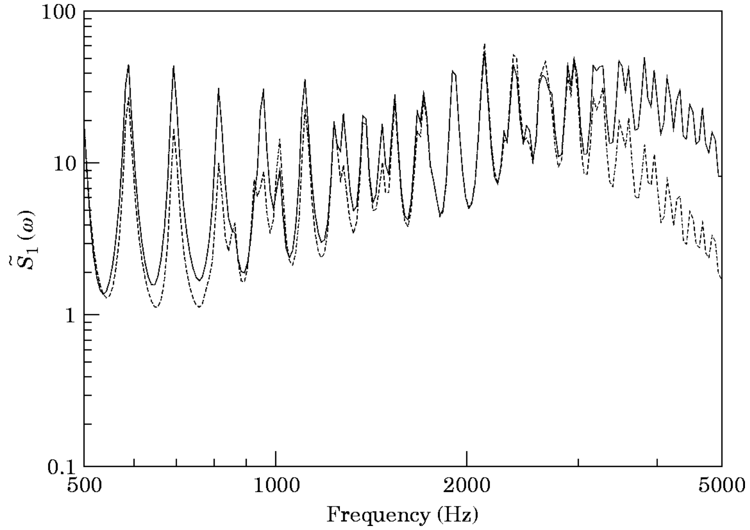

Figure 12. Case (a): sensitivity of the Chase I radiated power prediction to the choice of convection velocity: ——, U_c from equation (4.1); - - - -, $U_c = 0{\cdot}75U_\infty$.

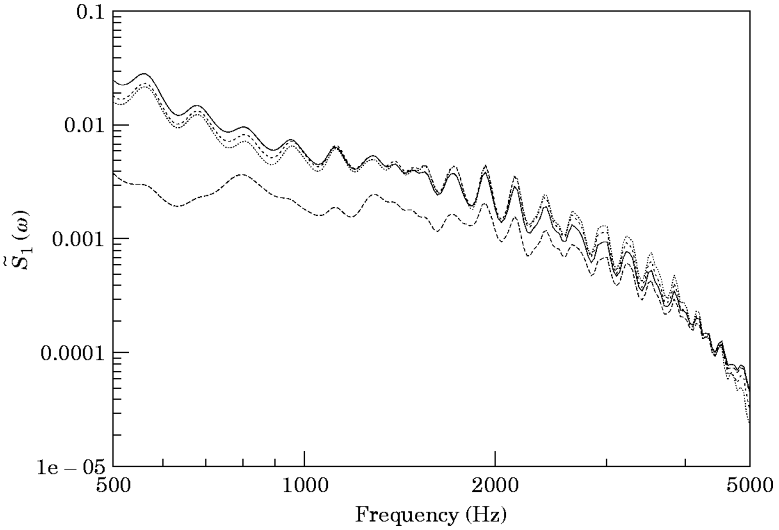

Figure 13. Radiated power spectra for case (a) with insulation and trim. ——, Corcos; – –, Efimtsov; - - - -, Smol'yakov and Tkachenko; · · · ·, Chase I.

by the corresponding calculation for the trimmed plate. One thus expects to observe the same behaviour in the model comparisons as for the bare plate, and this is confirmed by Figures 13–15, which are the trimmed plate analogues of Figures 10–12.

4.2.3. *Influence of the oblique spatial correlation function*

The customary assumption for oblique spatial pressure correlations is that they may be found from the product of the empirically determined longitudinal and lateral correlation functions, as in the Corcos and Efimtsov models. However, this assumption is challenged by Smol'yakov and Tkachenko, who combine the longitudinal and lateral separation arguments geometrically, rather than additively. It is therefore of interest to investigate

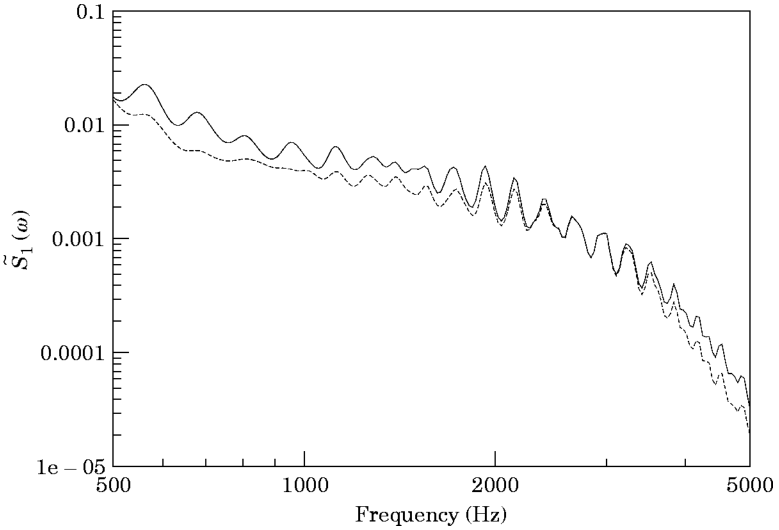

Figure 14. Case (a) with insulation and trim: sensitivity of the Smol'yakov and Tkachenko radiated power prediction to the choice of convection velocity: ——, U_c from equation (4.1); - - - -, $U_c=0{\cdot}8U_\infty$.

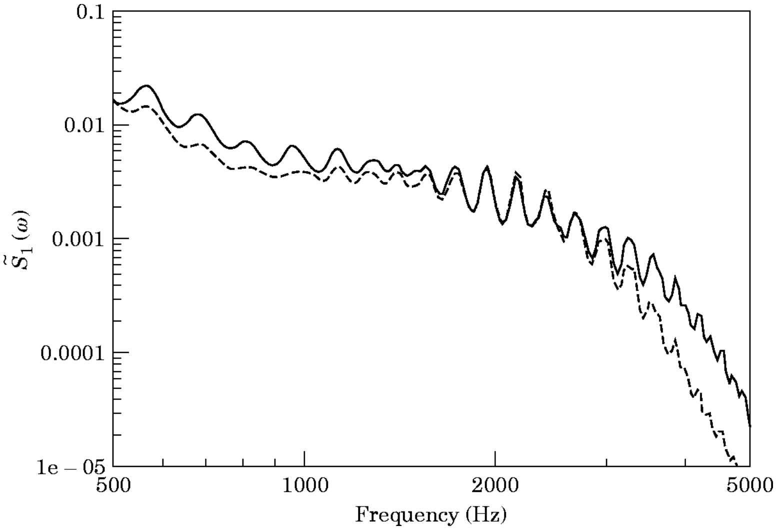

Figure 15. Case (a) with insulation and trim: sensitivity of the Chase I radiated power prediction to the choice of convection velocity: ——, U_c from equation (4.1); - - - -, $U_c = 0{\cdot}75\,U_\infty$.

how the choice of oblique correlation formulation affects the convective peak geometry, and hence the radiated sound power. To do so, one can discard the *ad hoc* low wavenumber correction terms (3.7) and (3.10) from the Smol'yakov and Tkachenko model, and write the basic results in terms of the correlation lengths Λ_y and Λ_z. This gives

$$\tilde{\Phi}_p(\mathbf{k},\omega) = \frac{\omega^2}{U_c^2}\frac{2\pi\Lambda_y\Lambda_z}{[1+\Lambda_z^2(k_z-\omega/U_c)^2+\Lambda_y^2k_y^2]^{3/2}}, \tag{4.2}$$

which may be compared directly with the Efimtsov spectrum

$$\tilde{\Phi}_p(\mathbf{k},\omega) = \frac{\omega^2}{U_c^2}\frac{4\Lambda_y\Lambda_z}{[1+\Lambda_z^2(k_z-\omega/U_c)^2][1+\Lambda_y^2k_y^2]}. \tag{4.3}$$

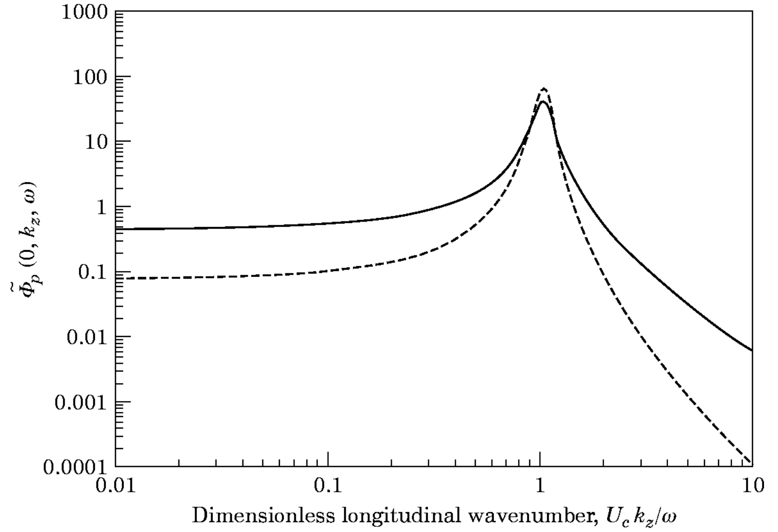

Figure 16. The effect of the oblique correlation formulation on the wavenumber–frequency spectrum for $Sh = 248$: ——, Standard formulation; - - - -, geometric formulation. The geometric formulation leads to a significantly narrower convective peak.

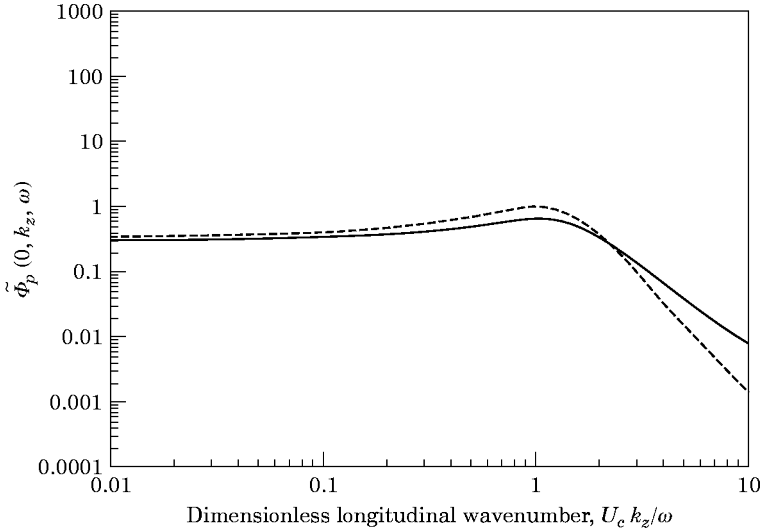

Figure 17. The effect of the oblique correlation formulation on the wavenumber–frequency spectrum for $Sh = 24{\cdot}8$: ——, Standard formulation; - - - -, geometric formulation. The differences between the two formulations are less marked at this frequency, due to the influence of the boundary layer thickness in limiting the correlation lengths.

The dependence of these spectra on k_z, for $k_y = 0$, and Λ_y and Λ_z given by Efimtsov's expressions, is plotted in Figures 16 and 17. At the higher frequency ($Sh = 248$, Figure 16), the results are similar to those of Figure 6, as the correlation lengths in the Smol'yakov and Tkachenko model nearly match those of the Efimtsov model. The main differences here are due to the omission of the low wavenumber correction term. However, at the lower frequency ($Sh = 24{\cdot}8$, Figure 17), the Efimtsov correlation lengths are much shorter, and the geometric formulation yields a significantly broader spectrum than the Smol'yakov and Tkachenko result of Figure 7. Note also that the contrast between the two

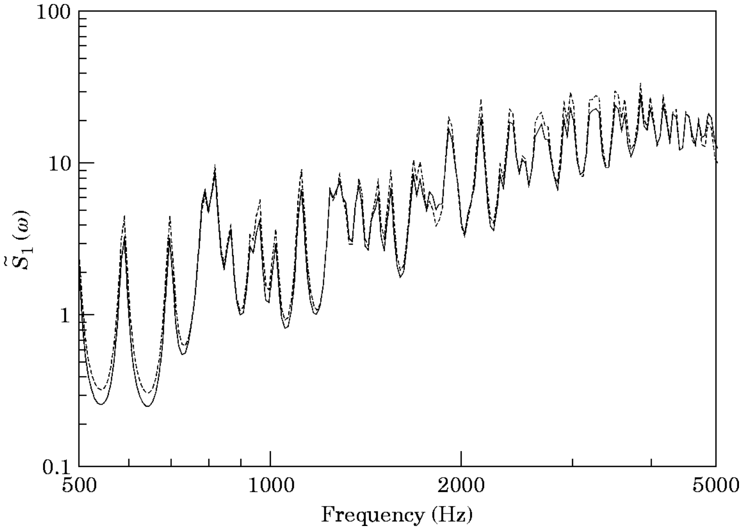

Figure 18. The effect of the oblique correlation formulation on the radiated power spectrum: ——, Standard formulation; - - - -, geometric formulation.

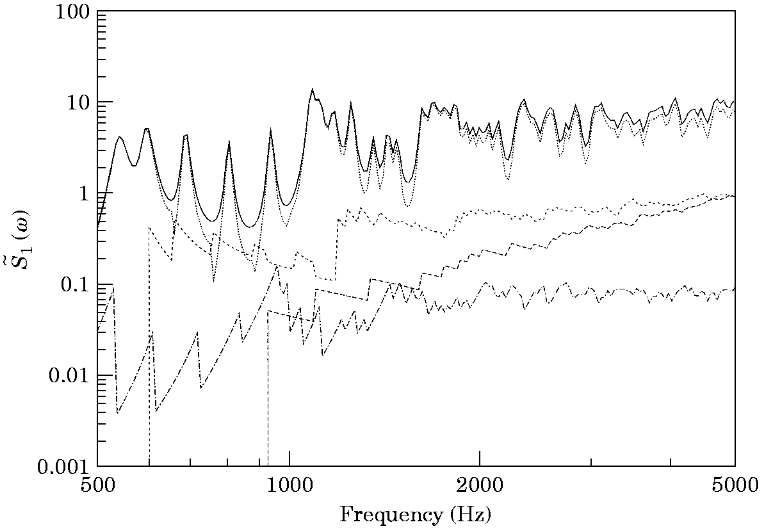

Figure 19. Radiated power spectrum by mode class for case (b), obtained by using the Efimtsov model: ——, Overall power; – –, efficient modes; - - - -, mass-limited modes; · · · ·, resonant modes; – · – · , stiffness-limited modes. The resonant mode contribution again dominates over the entire frequency range.

formulations is less marked here, due to the reduction in $\Lambda_z\ \omega/U_c$ imposed by the boundary layer thickness.

The influence of these differences on the radiated sound is evident in Figure 18, which shows similar trends to the original comparison (Figure 10). Although the effect is now less significant, the geometric formulation, with its narrower convective peak, still predicts a generally higher radiated sound power than the standard Efimtsov model.

4.3. TEST CASE (B)

For test case (a), it has been seen that it is the convective peak in $\tilde{\Phi}_p(\mathbf{k}, \omega)$ that determines the overall sound radiation, but that models which are all accepted as giving ‘correct’ levels there can still yield different results at higher frequencies, when the detailed shape of the peak becomes important. Additionally, the differing predictions for the convection velocity can affect spectrum levels significantly for models with narrow convective peaks. One can now move on to consider whether these conclusions are modified for case (b), where no hydrodynamic coincidence occurs.

As previously, one first considers the contributions to the radiated sound from the four mode classes defined in section 4.2.1. Although this case exhibits no hydrodynamic coincidence, the resonant modes are still found to dominate each model’s overall prediction, with the efficient and highly excited, stiffness-limited modes well down in comparison. (The breakdown for the Efimtsov model is shown in Figure 19.) The solutions for the different wavenumber–frequency spectrum models will thus reflect their low wavenumber behaviour, as is evident from Figure 20. The Efimtsov model still tends towards the Corcos model, as it should*, with the effect of its broader peak still tending to be a reduction in low frequency levels (although equally some mid-frequency levels are higher as a result). By comparison, the Smol’yakov and Tkachenko and Chase I models’ predictions are significantly lower, reflecting their reduced low wavenumber levels in $\tilde{\Phi}_p(\mathbf{k}, \omega)$. The difference between the low wavenumber behaviour of the two models is also

---

* Recall that the range of *Sh* is the same in cases (a) and (b).

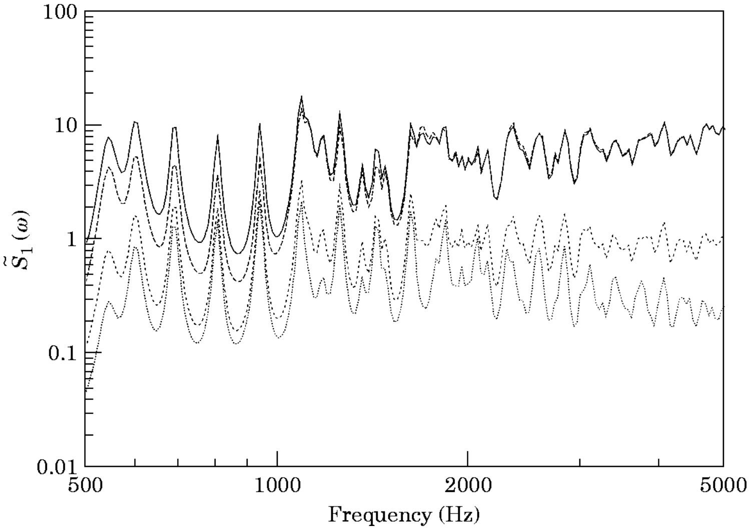

Figure 20. Radiated power spectra for case (b). ——, Corcos; – –, Efimtsov; - - - -, Smol'yakov and Tkachenko; · · · · , Chase I.

clearly reflected here. These results are similar to those obtained by Borisyuk [25], whose examples, like this test case, do not show hydrodynamic coincidence.

As with case (a), a different choice of convection velocity for the Smol'yakov and Tkachenko and Chase I models leads to noticeable differences in the radiated sound (see Figures 21 and 22), although here they are simply correlated with the size of the constant U_c in comparison to Efimtsov's value—the prediction is higher at low frequencies, and lower at high frequencies. This holds for both models, even though the Smol'yakov and Tkachenko wavenumber–frequency spectrum is flat at sufficiently low wavenumbers.

Again, as in case (a), the results for the trimmed plate correspond closely to those for the bare plate, and one may thus conclude that, for situations in which the convection

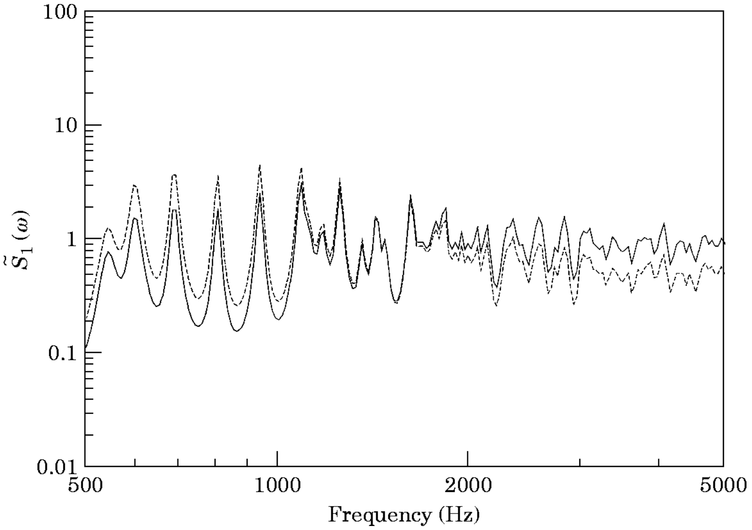

Figure 21. Case (b): sensitivity of the Smol'yakov and Tkachenko radiated power prediction to the choice of convection velocity: ——, U_c from equation (4.1); - - - -, $U_c = 0{\cdot}8\, U_\infty$.

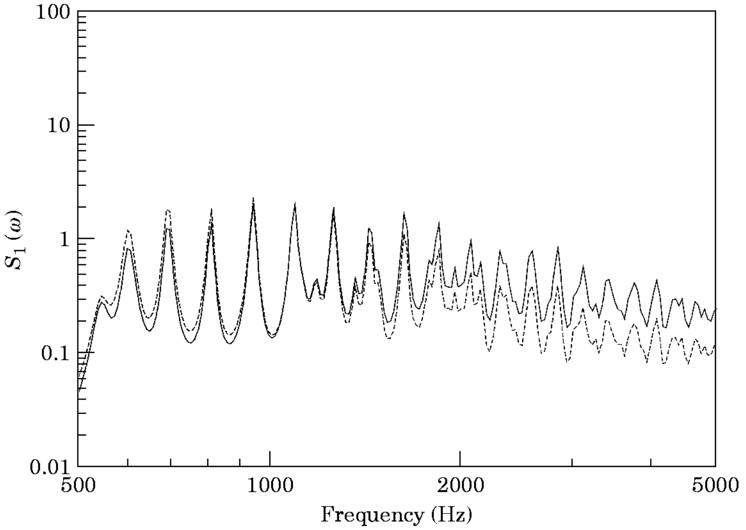

Figure 22. Case (b): sensitivity of the Chase I radiated power prediction to the choice of convection velocity: ——, U_c from equation (4.1); - - - -, $U_c = 0{\cdot}75\ U_\infty$.

velocity is significantly lower than the free wave speed in the structure, and hydrodynamic coincidence is therefore not found, the low wavenumber levels of the wavenumber–frequency spectrum model used are important, as equally is the choice of convection velocity.

5. CONCLUSIONS

In this paper the effect of differing choices of wavenumber–frequency spectrum model on the sound radiated by a boundary layer driven plate has been considered for two cases: the first, case (a), with parameters appropriate to a high speed subsonic civil aircraft, and the second, case (b), with a slightly stiffer structure and a significantly lower free-stream velocity. In case (a), resonant modes are also highly excited (hydrodynamic coincidence), while in case (b) they are driven by the low wavenumber region of the wavenumber–frequency spectrum. However, in each case their contributions are found to dominate the radiated power.

In case (a), then, it is the convective peak in the wavenumber–frequency spectrum which is significant, and for frequencies low enough for this peak to be narrow in comparison to the shape function peak, the predictions of different models coincide. However, at high frequencies, when the convective peak is broader, details of its shape become important, and models which are generally accepted to agree at convective wavenumbers yield different results. In particular, empirical models with identical longitudinal and lateral spatial correlation functions give varying predictions, depending on how the overall correlation function is formed. The width of the convective peak also determines the sensitivity of the results to the choice of convection velocity, with narrower peaks giving greater sensitivity.

In case (b) the resonant modes are driven by the low wavenumber region of the wavenumber–frequency spectrum, and it is important to achieve the correct behaviour here if predictions are to be reliable. Equally, the convection velocity must again be accurately specified, although it is now the slope of the low wavenumber region of the model spectrum that determines the sensitivity to this parameter. (This kind of dependence on U_c is also seen at frequencies above 4 kHz in case (a).)

Which, then, is the best model for the aircraft noise problem? Since this issue is most important for higher speed aircraft, one may assume that hydrodynamic coincidence will occur, and therefore that the key is to have an accurate description of the convective peak. The inability of the Corcos model to account for correlation length dependence on boundary layer thickness rules it out as a candidate, but Efimtsov's extension may well be suitable—a welcome conclusion, given that it is the only model among those considered here derived from aircraft rather than laboratory measurements. However, since the detailed shape of the convective peak has been found to be important, it may be necessary to abandon the multiplicative approach to forming the overall spatial correlation function from longitudinal and lateral correlation function measurements, admitted by Efimtsov [21] to give errors up to 30%, and turn to alternative formulations, such as that proposed by Smol'yakov and Tkachenko [22]. Further sophistication, though, is likely to be required only in cases which do not exhibit hydrodynamic coincidence.

REFERENCES

1. J. F. WILBY and F. L. GLOYNA 1972 *Journal of Sound and Vibration* **23**, 467–486. Vibration measurements of an airplane fuselage structure, II: jet noise excitation.
2. W. R. GRAHAM 1996 *Journal of Sound and Vibration* **192**, 101–120. Boundary layer induced noise in aircraft, part I: the flat plate model.
3. W. R. GRAHAM 1996 *Journal of Sound and Vibration* **192**, 121–138. Boundary layer induced noise in aircraft, part II: the trimmed flat plate model.
4. A. P. DOWLING 1983 *Journal of Fluid Mechanics* **128**, 181–198. Flow–acoustic interaction near a flexible wall.
5. M. S. HOWE 1992 *Journal of the Acoustical Society of America* **91**(1), 91–98. The wall-pressure spectrum in turbulent flow over a randomly inhomogeneous elastic solid.
6. H. G. DAVIES 1971 *Journal of the Acoustical Society of America* **49**(3), 878–889. Sound from turbulent-boundary-layer-excited panels.
7. B. M. EFIMTSOV and S. E. SHUBIN 1977 *Soviet Physics—Acoustics* **23**(4), 334–337. Experimental study of the vibrations and sound radiation of a plate in a turbulent pressure-fluctuation field.
8. B. M. EFIMTSOV, L. Y. KUDISOVA and A. A. LEBEDEV 1984 *Soviet Physics—Acoustics* **30**(5), 426–427. Experimental data on the vibrations and acoustic radiation of a plate in a field of turbulent pressure fluctuations at supersonic flow velocities.
9. B. M. EFIMTSOV 1986 *Soviet Physics—Acoustics* **32**(4), 336–337. Vibrations of a cylindrical panel in a field of turbulent pressure fluctuations.
10. S. BANO, R. MARMEY, L. JOURDAN and J.-P. GUIBERGIA 1992 *Journal d'Acoustique* **5**, 99–124. Etude theorique et experimentale de la reponse vibro-acoustique d'une plaque couplee a une cavite en fluide lourd.
11. A. FRENDI 1997 *American Institute of Aeronautics and Astronautics Journal* **35**, 58–66. Coupling between a supersonic turbulent boundary layer and a flexible structure.
12. S. F. WU and L. MAESTRELLO 1995 *American Institute of Aeronautics and Astronautics Journal* **33**, 13–19. Responses of finite baffled plate to turbulent flow excitations.
13. W. R. GRAHAM 1993 in *Proceedings of NOISE-CON* 93, 145–150. New York: Noise Control Foundation. Evaluation of a model for boundary-layer induced noise in aircraft.
14. W. R. GRAHAM 1995 *Philosophical Transactions of the Royal Society of London* **A352**, 1–43. High frequency vibration and acoustic radiation of fluid-loaded plates.
15. Y. F. HWANG and G. MAIDANIK 1990 *Journal of Sound and Vibration* **142**, 135–152. A wavenumber analysis of the coupling of a structural mode and flow turbulence.
16. G. M. CORCOS 1964 *Journal of Fluid Mechanics* **18**(3), 353–378. The structure of the turbulent pressure field in boundary-layer flows.
17. W. K. BLAKE 1986 *Mechanics of Flow-induced Sound and Vibration*, *Volume II: Complex Flow–Structure Interactions*. New York: Academic Press.
18. D. M. CHASE 1980 *Journal of Sound and Vibration* **70**, 29–67. Modeling the wavevector–frequency spectrum of turbulent boundary layer wall pressure.
19. D. M. CHASE 1987 *Journal of Sound and Vibration* **112**, 125–147. The character of the turbulent wall pressure spectrum at subconvective wavenumbers and a suggested comprehensive model.

20. J. E. Ffowcs Williams 1982 *Journal of Fluid Mechanics* **125**, 9–25. Boundary-layer pressures and the Corcos model: a development to incorporate low wavenumber constraints.
21. B. M. Efimtsov 1982 *Soviet Physics—Acoustics* **28**(4), 289–292. Characteristics of the field of turbulent wall pressure fluctuations at large Reynolds numbers.
22. A. V. Smol'yakov and V. M. Tkachenko 1991 *Soviet Physics—Acoustics* **37**(6), 627–631. Model of a field of pseudosonic turbulent wall pressures and experimental data.
23. W. V. Bhat 1971 *Journal of Sound and Vibration* **14**(4), 439–457. Flight test measurement of exterior turbulent boundary-layer pressure fluctuations on Boeing Model 737 airplane.
24. Y. F. Hwang and F. E. Geib 1984 *Transactions of the American Society of Mechanical Engineers*, *Journal of Vibration*, *Acoustics*, *Stress and Reliability in Design* **106**, 334–342. Estimation of the wavevector-frequency spectrum of turbulent boundary layer wall pressure by multiple linear regression.
25. A. A. Borisyuk 1994 *Acoustical Physics* **40**(6), 798–802. Acoustic radiation of an elastic rectangular plane excited by a turbulent boundary layer.